Bioactive Materials 34 (2024) 414–421

Contents lists available at ScienceDirect

Bioactive Materials

journal homepage: www.keaipublishing.com/en/journals/bioactive-materials

pH/GSH dual responsive nanosystem for nitric oxide generation enhanced type I photodynamic therapy

Jianhua Zou [a,b], Zheng Li [a,b], Yang Zhu [a,b], Yucen Tao [a,b], Qing You [a,b], Fangfang Cao [a,b], Qinghe Wu [a,b], Min Wu [e,**], Junjie Cheng [a,f,***], Jianwei Zhu [a,g,****], Xiaoyuan Chen [a,b,c,d,*]

[a] Departments of Diagnostic Radiology, Surgery, Chemical and Biomolecular Engineering, and Biomedical Engineering, Yong Loo Lin School of Medicine and College of Design and Engineering, National University of Singapore, Singapore, 119074, Singapore
[b] Nanomedicine Translational Research Program, NUS Center for Nanomedicine, Yong Loo Lin School of Medicine, National University of Singapore, Singapore, 117597, Singapore
[c] Clinical Imaging Research Centre, Centre for Translational Medicine, Yong Loo Lin School of Medicine, National University of Singapore, Singapore, 117599, Singapore
[d] Institute of Molecular and Cell Biology, Agency for Science, Technology, and Research (A*STAR), 61 Biopolis Drive, Proteos, Singapore, 138673, Singapore
[e] Department of Plastic and Reconstructive Surgery, Shanghai Ninth People's Hospital, Shanghai Jiaotong University, Shanghai, 200011, PR China
[f] Department of Chemistry Center for Bioanalytical Chemistry, University of Science and Technology of China, Hefei, 230026, PR China
[g] College of Life Science, Nanjing Normal University, 1 Wenyuan Road, Nanjing, 210023, PR China

ARTICLE INFO

Keywords:
TME responsive
NO gas therapy
NIR-II imaging
Type I PDT

ABSTRACT

Tumor hypoxia diminishes the effectiveness of traditional type II photodynamic therapy (PDT) due to oxygen consumption. Type I PDT, which can operate independently of oxygen, is a viable option for treating hypoxic tumors. In this study, we have designed and synthesized JSK@PEG-IR820 NPs that are responsive to the tumor microenvironment (TME) to enhance type I PDT through glutathione (GSH) depletion. Our approach aims to expand the sources of therapeutic benefits by promoting the generation of superoxide radicals ($O_2^{-\cdot}$) while minimizing their consumption. The diisopropyl group within PEG-IR820 serves a dual purpose: it functions as a pH sensor for the disassembly of the NPs to release JSK and enhances intermolecular electron transfer to IR820, facilitating efficient $O_2^{-\cdot}$ generation. Simultaneously, the release of JSK leads to GSH depletion, resulting in the generation of nitric oxide (NO). This, in turn, contributes to the formation of highly cytotoxic peroxynitrite ($ONOO^{-\cdot}$), thereby enhancing the therapeutic efficacy of these NPs. NIR-II fluorescence imaging guided therapy has achieved successful tumor eradication with the assistance of laser therapy.

1. Introduction

Hypoxia, a frequently encountered obstacle in cancer, is closely linked to invasiveness, tumorigenesis, recurrence, and metastasis [1]. Oxygen deficiency, a significant detrimental factor, compromises cancer therapy, leading to unfavorable clinical outcomes [2]. The presence of low pH in the tumor microenvironment (TME) underscores the importance of creating smart anti-cancer medications, which is crucial in maximizing treatment effectiveness while minimizing potential side effects [2]. Photodynamic therapy (PDT) offers several advantages, including noninvasiveness [3], minimal drug resistance [4], precise spatiotemporal control [5], and the potential to induce immunogenic cell death (ICD), thereby triggering an antitumor immune response. These qualities hold significant promise for clinical cancer treatment

Peer review under responsibility of KeAi Communications Co., Ltd.

* Corresponding authors. Departments of Diagnostic Radiology, Surgery, Chemical and Biomolecular Engineering, and Biomedical Engineering, Yong Loo Lin School of Medicine and College of Design and Engineering, National University of Singapore, Singapore, 119074, Singapore.
** Corresponding author.
*** Corresponding authors. Departments of Diagnostic Radiology, Surgery, Chemical and Biomolecular Engineering, and Biomedical Engineering, Yong Loo Lin School of Medicine and College of Design and Engineering, National University of Singapore, Singapore, 119074, Singapore.
**** Corresponding author. Departments of Diagnostic Radiology, Surgery, Chemical and Biomolecular Engineering, and Biomedical Engineering, Yong Loo Lin School of Medicine and College of Design and Engineering, National University of Singapore, Singapore, 119074, Singapore.
E-mail addresses: wmviola@alumni.sjtu.edu.cn (M. Wu), jjcheng2017@ustc.edu.cn (J. Cheng), jianweizhu@njnu.edu.cn (J. Zhu), chen.shawn@nus.edu.sg (X. Chen).

https://doi.org/10.1016/j.bioactmat.2023.12.023
Received 7 October 2023; Received in revised form 8 December 2023; Accepted 25 December 2023

[6]. Traditional PDT typically relies on the generation of cytotoxic singlet oxygen ($^1O_2$) through a direct energy transfer process, known as the type II process [3a,7]. However, this process heavily relies on the availability of molecular oxygen during blood circulation. Consequently, the therapeutic effectiveness of type II PDT is often unsatisfactory as it not only consumes oxygen but also damages blood vessels, worsening hypoxia [4b,4c].

In contrast to type II PDT, type I PDT induces the generation of free radicals, including hydroxyl radicals ($OH^{-}\cdot$) and superoxide radicals ($O_2^{-}\cdot$), through electron/hydrogen transfer from triplet excited photosensitizers (PSs) [8]. Type I photosensitizers (PSs) are less reliant on oxygen and offer greater promise for treating hypoxic tumors. Recent advancements have supported this notion, highlighting their potential [9], benefiting from reactions like the Franck-Condon reaction or intracellular superoxide dismutase (SOD)-mediated disproportionation.

Nitric oxide (NO), a gaseous signaling molecule naturally present in the human body, plays a pivotal role in regulating processes like vascular relaxation and immune responses [10]. It has also found applications in the treatment of conditions such as tumors, bacteria/biofilms, wounds, and hepatic ischemia-reperfusion injury [11]. However, delivering NO precisely has always been a challenge due to its uncontrollable release into the bloodstream and its short half-life (less than 5 s) [10,12,13].

Capitalizing on the advancements in nanomedicine, we have devised a sophisticated nanosystem called JSK@PEG-IR820 for the purpose of delivering nitric oxide (NO) and enabling type I PDT, as illustrated in Scheme 1. This nanosystem is composed of three crucial components: a pH-responsive group (diisopropyl), a photo-responsive molecule (IR820), and a NO precursor (O2-(2,4-dinitrophenyl) 1-[(4-ethoxycarbonyl)piperazin-1-yl]diazen-1-ium-1,2-diolate, referred to as JSK). Our approach seeks to 'broaden sources' by enhancing electron transfer for the generation of superoxide radicals ($O_2^{-}\cdot$) and 'reduce expenditure' by diminishing $O_2^{-}\cdot$ consumption. The diisopropyl group serves as a pH sensor, triggering the nanosystem's disassembly to release JSK. It also facilitates efficient superoxide radical generation through enhanced electron transfer. Furthermore, JSK functions as a pro-drug capable of depleting the reductive glutathione (GSH), thus reducing $O_2^{-}\cdot$ consumption and enhancing type I PDT. This process also leads to the production of highly cytotoxic peroxynitrite ($ONOO^{-}$) through the reaction between $O_2^{-}\cdot$ and NO.

Leveraging the advantages of NIR-II fluorescence imaging, such as low background, high resolution, and deep tissue penetration [14], JSK@PEG-IR-820 NPs enable precise navigation to the tumor site, favoring the synergistic PDT/NO therapy against Uppsala 87 malignant glioma (U87MG)[30-33]. *In vitro* confocal laser scanning microscopy (CLSM) has demonstrated efficient generation of $O_2^{-}\cdot$ and $ONOO^{-}\cdot$ using DHR123 and O31 as probes, respectively. Moreover, the half-maximal inhibitory concentration (IC_{50}) of JSK@PEG-IR820 has been significantly reduced. Complete tumor regression has been achieved with laser assistance, while sparing normal tissues, underscoring the high phototoxicity and excellent biocompatibility of these NPs.

2. Experimental section

2.1. Materials and apparatus

Poly(ethylene glycol)-amine (PEG-NH_2), 2-(diisopropylamino)ethyl methacrylate (99 %), azobisisobutyrontrile (AIBN, 98 %), thiazolyl blue tetrazolium bromide (MTT, 97.5 %), 2-[2-[2-chloro-3-[[1,3-dihydro-1,1-dimethyl-3-(4-sulfobutyl)-2H-benzo[e]indol-2-ylidene]-ethylidene]-1-cyclohexen-1-yl]-ethenyl]-1,1-dimethyl-3-(4-sulfobutyl)-1H-benzo[e]indolium hydroxide inner salt (IR820, 80 %), O2-(2,4-dinitrophenyl) 1-[(4-ethoxycarbonyl)piperazin-1-yl]diazen-1-ium-1,2-diolate (JSK, 99 %), ethyl ether (99.9 %), dimethylformamide (DMF, 99.5 %) and tetrahydrofuran (THF) were purchased from Sigma-Aldrich. 1-(chloromethyl)-4-vinylbenzene, 4-cyano-4-(phenylcarbonothioylthio) pentanoic acid N-succinimidyl ester (CPPA) were purchased from Adamas and were used without further purification. The ^{1}HNMR and ^{13}CNMR spectra were measured on Bruker DRX NMR spectrometer at 298 K as the internal standard with solvent residual (400 MHz). UV–vis

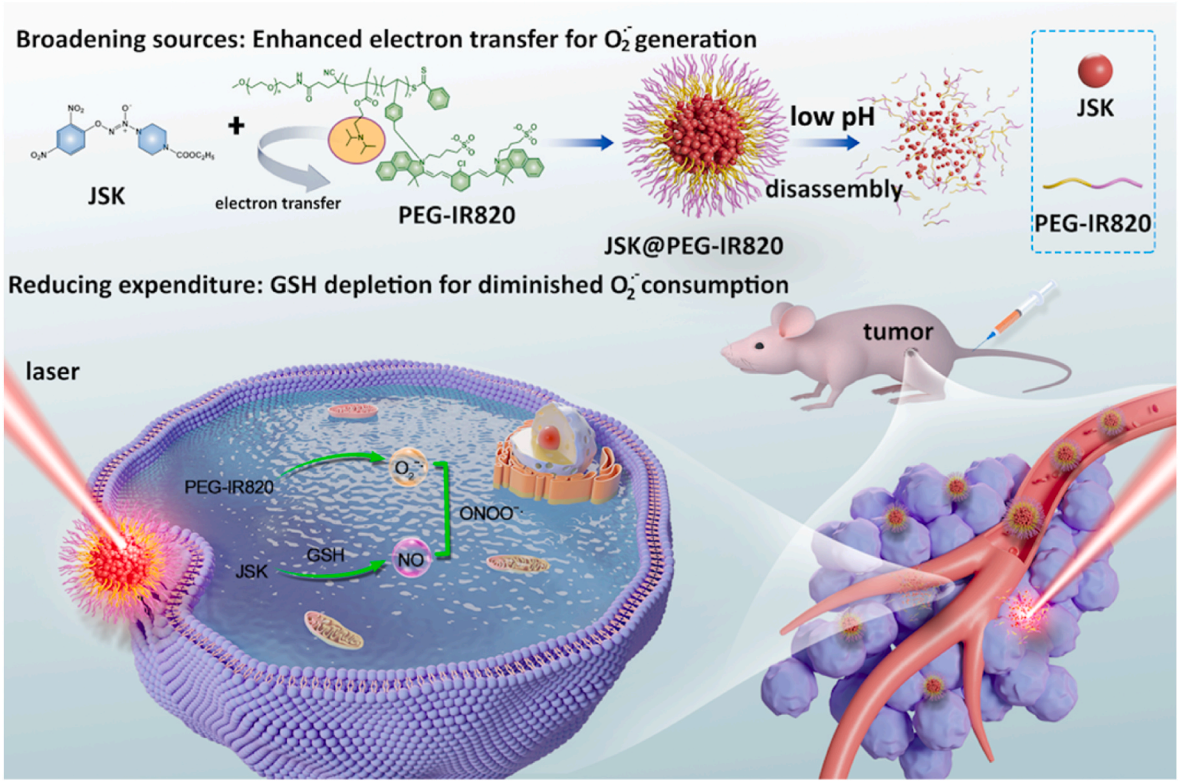

Scheme 1. Illustration of synthesis of JSK@PEG-IR820 nanosystem for pH triggered JSK release and GSH activated NO therapy enhanced type I PDT.

spectra were recorded on a UV-Vis-NIR spectrophotometer (Agilent, Carry 5000). Fluorescence spectra were measured on an FS500 spectrometer (Edinburgh, UK). Dynamic light scattering (DLS) was measured on a Litesizer 500 size analyzer. Transmission electron microscope (TEM) images were measured on equipment of JEOL JEM-2100.

2.2. Synthesis of PEG-IR820

A mixture of PEG-NH_2 (200 mg, 0.1 mmol) and 3 mL dichloromethane (DCM) was added to a mixture of CPAA (56.4 mg, 0.15 mmol) and DCM (5 mL). With the catalysis of triethylamine (TEA, 4 μL, 0.0288 mmol) reaction for 24 h at room temperature, the crude product was condensed by rotary evaporator and precipitated in cold ethyl ether to obtain PEG-CPPA. Then reversible addition-fragmentation chain transfer (RAFT) polymerization was used to conjugate 2-(diisopropylamino) ethyl methacrylate and 1-(chloromethyl)-4-vinylbenzene using AIBN as the initiator (Fig. S1). PEG-CPPA (100 mg, 0.04 mmol), monomer 1-(chloromethyl)-4-vinylbenzene (365 mg, 2.4 mmol), AIBN (1.00 mg, 0.006 mmol) were dissolve in 1,4-dioxane (5 mL) completely and added to a flask with stirring. After purging with nitrogen for about 20 min, the flask was sealed and moved to oil bath at 70 °C for 2 d. PEGN could be obtained after precipitation in cold ethyl ether. Then a mixture of PEGN (200 mg, 0.045 mmol), IR820 (382 mg, 0.45 mmol), K_2CO_3 (93 mg, 0.675 mmol), KI (8 mg, 0.045 mmol) was dissolved in DMF (20 mL) and heated at 70 °C for one day. PEG-IR820 was obtained by the dialysis of the crude product against water and freeze drying for 2 days. Finally, 2-(diisopropylamino)ethyl methacrylate (511 mg, 2.4 mmol) was conjugated to prepare PEG-IR820 with the similar RAFT reaction.

2.3. Synthesis and characterization of JSK@PEG-IR820 nanoparticles (NPs)

A mixture of JSK (2 mg) and PEG-IR820 (10 mg) was dissolved in THF (1 mL) with ultrasound. Then the mixture was added dropwise to a mixture of water (5 mL) and THF (1 mL) with ultrasound. THF was removed by nitrogen bubbling for 20 min in the fume hood. Eventually JSK@PEG-IR820 NPs were obtained and stored in dark condition. The product was freeze-dried for further use.

2.4. Calculation of drug loading content (DLC), drug loading efficiency (DLE) and drug release

DLC and DLE were measured by UV–Vis and calculated according to the following equations:

$$\text{DLC (wt.\%)} = \text{mass of loaded drug /total mass of loaded drug and polymer} \times 100\% \quad (1)$$

$$\text{DLE (\%)} = \text{mass of loaded drug/mass of theoretical drug} \times 100\% \quad (2)$$

Drug release was calculated by recording the absorbance of JSK. First, the standard curve was investigated by recording the absorbance of JSK under different concentrations. JSK@PEG-IR820 NPs (JSK concentration: 400 μg/mL) were dissolved in PBS (1 mL) with different pH (7.4 and 6.5). Then the solution was dialyzed with dialysis bags (Mw 2000) in PBS (2 mL) with different pH (7.4 and 5.5). The absorbance of the solution was recorded, and the concentration was calculated according to the standard curve.

2.5. Superoxide radical, NO and ONOO-. generation detection

$O_2^{\cdot-}$, NO and $ONOO^{-\cdot}$ were detected by DHR123, DAF-FM and O31 probe, respectively. Generally, the fluorescence of a mixture of DHR123 (10 μM) and PEG-IR820 was recorded with or without laser irradiation, respectively. For the detection of NO, the fluorescence spectra of a mixture of DAF-FM (10 μM) and JSK and glutathione (5 mM) were measured at different time intervals. And a mixture of O31 (10 μM), glutathione (5 mM) and JSK@PEG-IR820 (10 μM) in PBS (5.5) was irradiated for the detection of $ONOO^-$.

2.6. Cell culture, cellular uptake and fluorescence imaging of cellular ROS

U87MG cells were cultured with a mixture of Dulbecco's modified Eagle's medium (DMEM, Gibco), 10 % fetal bovine serum (FBS) and 1 % penicillin-streptomycin at 37 °C under an atmosphere of 5 % CO_2. PEG-IR820, JSK and JSK@PEG-IR820 NPs were incubated with U87MG cells in a confocal dish for 24 h, respectively. Then the medium was discarded and the cells were washed by PBS (1 mL) 3 times. Polyoxymethylene (1 mL) was added to the culture for 25 min. Then polyoxymethylene was discarded, and the cells were washed with PBS three times. The samples incubated with PEG-IR820, JSK and JSK@PEG-IR820 were further incubated with DHR123 (10 μM), DAF-FM and O31 for another 3 min, respectively. The media were discarded, followed by washing with PBS (1 mL) three times. The control group and the one incubated with JSK were not irradiated exceptionally while the samples with PEG-IR820 or JSK@PEG-IR820 NPs were irradiated by laser (808 nm, 0.5 W/cm^2) for 1 min.

For the cellular uptake study, the samples were excited at 633 nm and the fluorescence was collected from 650 to 750 nm on a microscope (Olympus IX 70 inverted microscope). The samples co-incubated with JSK@PEG-IR820 and DHR123, DAF-FM and O31 were excited with 488 nm laser and the fluorescence collection ranges from 490 to 650 nm.

2.7. MTT assay and flow cytometry

U87MG cells were cultured in a 96-well plate and exposed to varying concentrations of PEG-IR820, JSK, and JSK@PEG-IR820. In the control group, cells were cultivated without any nanomaterials, while in the other groups, they were exposed to PEG-IR820, JSK, and JSK@PEG-IR820, respectively. After a 24-h incubation period, the cells in the dark group were not subjected to any exceptional irradiation, whereas those in the photo group were exposed to laser light (808 nm, 0.5 W/cm^2) for 5 min. Subsequently, MTT in PBS (5 mg/mL, 20 μL) was introduced into each well and allowed to incubate for an additional 4 h. The culture medium was then removed, and DMSO (200 μL) was added. The absorbance was measured at 492 nm using a Thermo Multiskan Mk3 Microplate Reader. The cell growth inhibitory effects were calculated by the following equation (2):

$$\text{Cell viability (\%)} = (A_{treatment} / A_{control}) \times 100\ \% \quad (3)$$

2.8. Annexin V-FITC/propidium iodide (PI) staining

U87MG cells were seeded in 6-well plates and subsequently divided into five distinct groups: the control group, JSK only, PEG-IR820 with/without irradiation and JSK@PEG-IR820 with irradiation. Cells were exposed to the corresponding nanoparticles at a concentration of 3.2 μg/mL. However, the photo group received an exceptional 5-min laser irradiation (808 nm, 0.5 W/cm^2), while the dark and JSK only groups did not. The apoptosis of U87MG cells was assessed using Annexin V-FITC/propidium iodide (PI) dual staining. The cells were collected and stained using the Annexin V-FITC/PI Cell Apoptosis Detection Kit (KeyGen Biotech, Nanjing, China) following the standard protocol. The apoptosis rates of the cells were quantified using a flow cytometer (BD Biosciences, San Jose, CA, USA).

2.9. In vivo NIR-II fluorescence imaging guided NO gas therapy enhanced type I PDT

Approval for animal experimentation was obtained from the Animal Center of Nanjing Normal University, Nanjing, China (IACUC-

20230226). Female nude mice were procured and subsequently injected with U87MG cells to establish tumors. For NIR-II fluorescence imaging, mice were intravenously administered JSK@PEG-IR820 NPs, and images were captured at various time points. After 48 h post-injection, the mice were humanely euthanized, and the NIR-II fluorescence intensity was measured in various organs, including the tumor, heart, liver, lungs, kidneys, and spleen.

In the treatment study, once the tumor volume reached approximately 80 mm^3, the mice were randomly divided into five groups (n = 4/group). The control group received a saline injection (100 μL) followed by laser irradiation (0.5 W/cm^2). The other four treatment groups received injections as follows: PEG-IR820 (1 mg/mL, 100 μL) alone, PEG-IR820 (1 mg/mL, 100 μL) with laser, JSK (200 μg/mL, 100 μL) alone, and JSK@PEG-IR820 with laser (1 mg/mL, 100 μL). After 24 h of administration, only the tumors in the control group, the PEG-IR820 + laser group, and the JSK@PEG-IR820 + laser group were subjected to an 8-min laser irradiation (808 nm, 0.5 W/cm^2). Subsequently, the tumor volume and the mice's body weight were monitored every two days. The process above was repeated until the tumors disappeared. All of the nude mice were eventually euthanized, and a histological examination of their tumor, heart, liver, lungs, kidneys, and spleen was conducted. The organs from each mouse were carefully removed and fixed in a 4 % formaldehyde solution. Following dehydration, the tissues were embedded in paraffin cassettes and stained using hematoxylin and eosin (H&E) for histopathological analysis. Additionally, various hematological parameters, including red blood cell count, white blood cell count, platelet count, lymphocyte count, albumin levels, glucose levels, aspartate aminotransferase, alanine aminotransferase, alkaline phosphatase, total protein, blood urea nitrogen, and creatinine, were assessed.

2.10. Statistical analysis

Quantitative data were presented as mean ± standard deviation. Significant differences between groups were indicated by $*p < 0.05$, $**p < 0.005$ and $***p < 0.001$, respectively.

3. Results and discussions

3.1. Synthesis and general characterization of JSK@PEG-IR820 NPs

PEG-IR820 was synthesized through a three-step process (Fig. S1), and both the intermediate and final products were characterized using ^{1}HNMR and GPC (refer to Figs. S2 and S3). Next, JSK, serving as the NO precursor, was encapsulated within PEG-IR820 using a nanoprecipitation technique to produce water-dispersible JSK@PEG-IR820 nanoparticles. PEG-IR820 exhibited distinctive peaks at 697 and 825 nm (Fig. 1a). In contrast, a red shift was observed in the absorption spectrum of JSK@PEG-IR820 NPs (780 and 835 nm), which can be attributed to the *J*-aggregation of the nanoparticles. Fluorescence imaging in the NIR-II region offers a high signal-to-background ratio, as it experiences less tissue scattering and allows for greater penetration depth compared to NIR-I imaging [14]. Consequently, the emission spectrum of JSK@PEG-IR820 was recorded, revealing a broad emission ranging from 950 to approximately 1200 nm, indicating its potential for NIR-II imaging (Fig. 1b). The drug loading content (DLC) and drug loading efficiency (DLE) were 16.7 % and 50.0 %, respectively.

Due to the pH-responsive nature of the diisopropyl group, the dynamic light scattering (DLS) and transmission electron microscopy (TEM) were assessed in different buffers (pH 7.4 and 6.5). In pH 7.4 buffer, JSK@PEG-IR820 NPs displayed a uniform spherical morphology with an average diameter of 142 nm (Fig. 1c and d). However, under low pH conditions (6.5), the nanostructure underwent collapse, resulting in the disappearance of the spherical morphology and a reduction in particle size to approximately 63 nm (Fig. 1e and f). This observation highlights the potential of these NPs for pH-triggered drug release. Importantly, both PEG-IR820 and JSK@PEG-IR820 exhibited improved photostability, as no absorbance decay was observed after irradiation, unlike free IR820 (808 nm, 0.5 W/cm^2, 8 min, Fig. S4).

3.2. Superoxide radical, nitric oxide and peroxynitrite anion detection

We conducted investigations into the generation ability of superoxide radicals, nitric oxide, and $ONOO^-$ using DHR123, DAF-FM, and O31

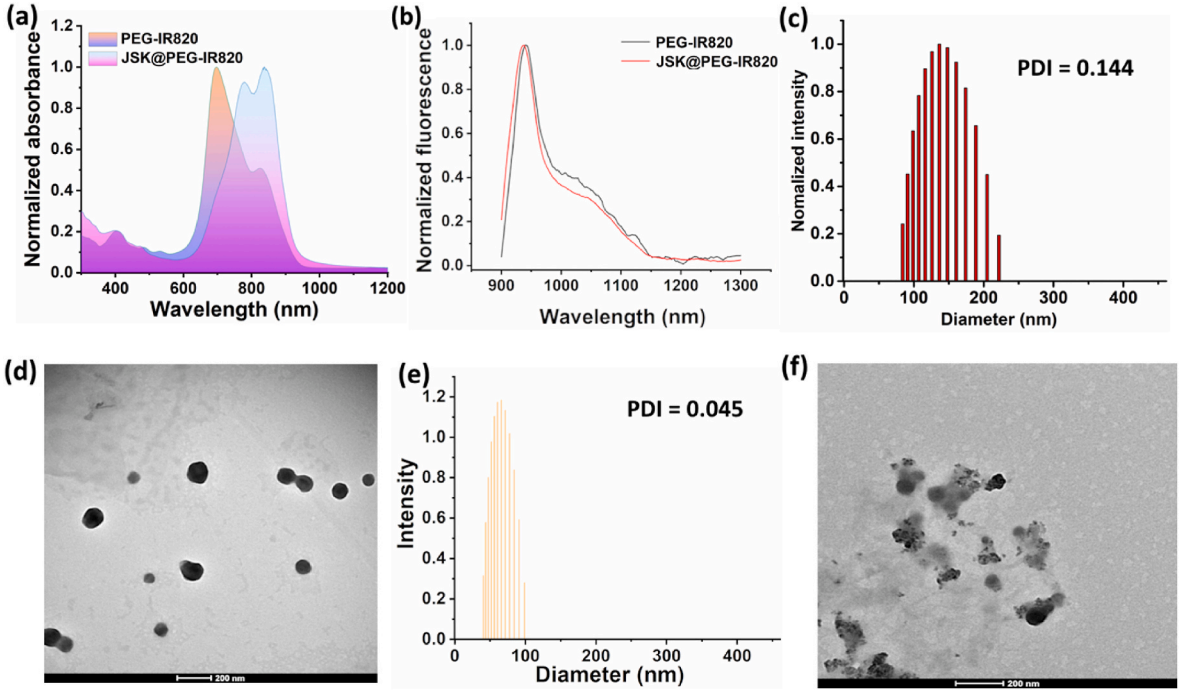

Fig. 1. (a) Normalized absorbance of PEG-IR820 and JSK@PEG-IR820 NPs. (b) Normalized emission spectra of free IR820 and JSK@PEG-IR820 NPs in water. (c) DLS and (d) TEM of JSK@PEG-IR820 NPs in buffer (pH 7.4). (e) DLS and (f) TEM of JSK@PEG-IR820 NPs in buffer (pH 6.5).

probes, respectively. The production of high levels of reactive oxygen species (ROS), particularly superoxide radicals during the type I process, holds the potential for inducing significant phototoxicity, leading to effective cell apoptosis. Therefore, DHR123 was employed as a probe due to its specific reactivity with superoxide radicals, causing it to transition from a non-fluorescent to a fluorescent state, as depicted in Fig. 2a. Following laser irradiation, the fluorescence intensity of DHR123 increased by approximately eightfold, while that of the control group exhibited a mere 1.7-fold increase, which is nearly negligible (Fig. 2b and c). This phenomenon can be attributed to the robust internal electron transfer from the diisopropyl group to IR820.

Within the tumor microenvironment (TME), the presence of highly reductive glutathione (GSH) can consume the ROS generated during PDT, compromising its therapeutic effectiveness. JSK, serving as a NO precursor, undergoes a two-step oxidation-reduction reaction due to the presence of (2,4-dinitrophenyl)-λ1-oxidane and 4λ2-piperazine-1-carboxylic acid, which can act as leaving groups while consuming GSH (Fig. 2d). We confirmed the NO generation capability of JSK@PEG-IR820 by observing the fluorescence enhancement of the commercially available probe DAF-FM (Fig. 2e). In the presence of GSH, the fluorescence intensity increased by nearly threefold compared to the control group (Fig. 2f). We mimicked the pH-triggered release of JSK in the TME by measuring the absorbance of GSH under varying pH conditions at different time intervals (Fig. 2g). Under neutral conditions, JSK release was limited (below 20 %). However, in an acidic environment, drug release was significantly accelerated (almost 80 %), owing to the specific responsiveness of the diisopropyl group to acidity. Finally, we characterized the generation of $ONOO^{-\cdot}$ by recording the fluorescence of the O31 probe in the presence of GSH with or without irradiation. The fluorescence of O31 was noticeably heightened because of the generation of $ONOO^{-\cdot}$ between the reaction of superoxide radicals and NO (Fig. 2h), whereas negligible fluorescence enhancement was observed in the control group (Fig. 2i).

3.3. *In vitro cellular uptake, ROS generation, MTT assay, and flow cytometry*

Efficient cellular uptake is a critical factor in determining the therapeutic effectiveness of JSK@PEG-IR820. To assess this, we utilized confocal laser scanning microscopy (CLSM) to examine the cellular uptake of JSK@PEG-IR820 by U87MG cells and to investigate the generation of ROS or RNS (reactive nitrogen species) using different probes. The red channels in Fig. 3a clearly indicate the effective cellular uptake of JSK@PEG-IR820, while the photogenerated superoxide radicals were confirmed by the activation of the green channel with DHR123. Furthermore, the generation of NO and $ONOO^{-\cdot}$ was evident from the

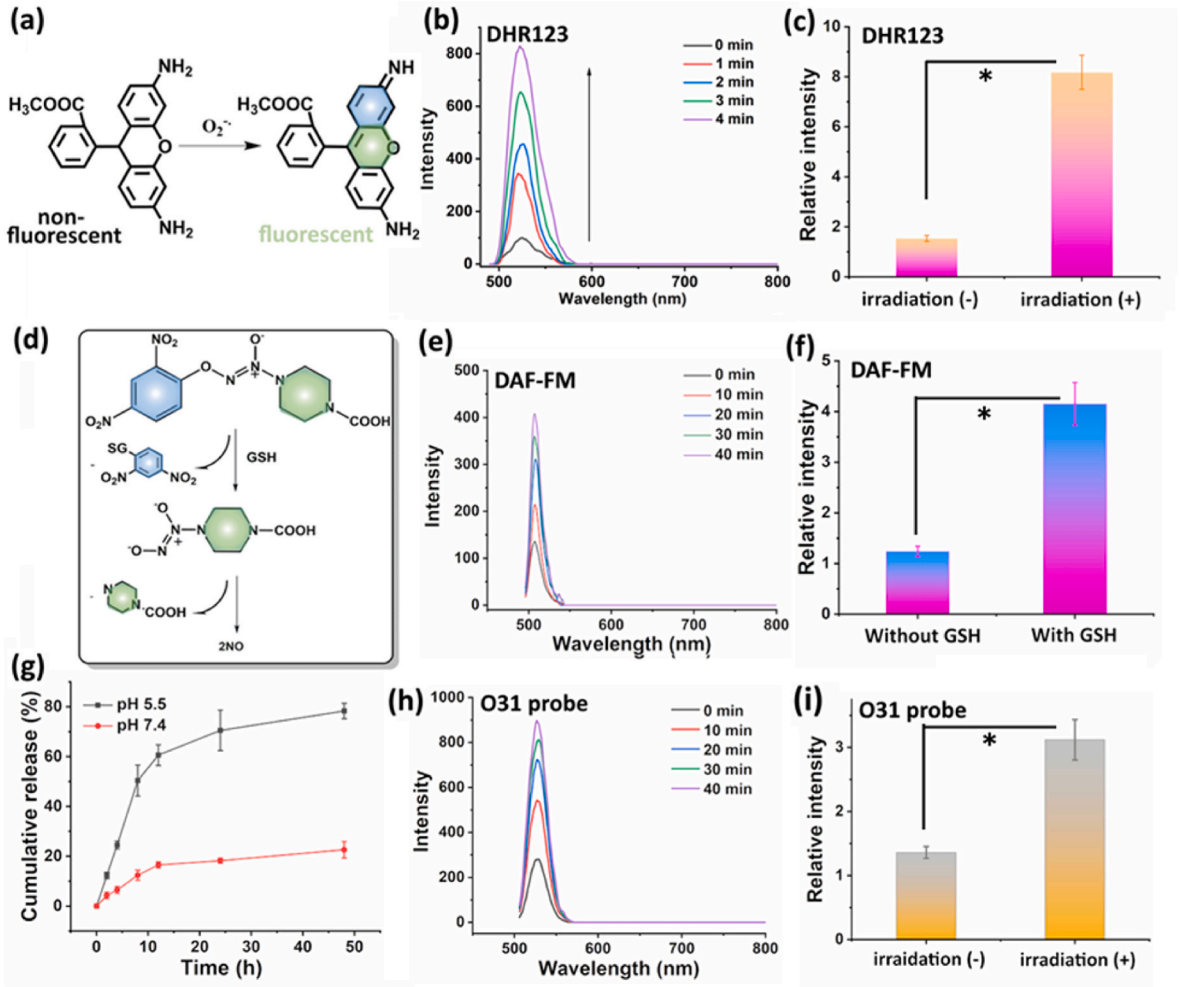

Fig. 2. (a) Mechanism of DHR123 as an indicator for superoxide radical generation. (b) Fluorescence intensity of DHR123 in the presence of NPs with laser irradiation (808 nm, 0.5 W/cm^2). (c) Comparison of the DHR123 fluorescence intensity with/without irradiation (n = 3). (d) Mechanism of JSK as a NO precursor for GSH induced NO generation. (e) Fluorescence intensity of DAF-FM in the presence of GSH (5 mM). (f) Comparison of the DAF-FM fluorescence intensity with/without GSH (n = 3). (g) JSK release under different pH (7.4 and 6.5). (h) Fluorescence intensity of O31 probe in the presence of NPs and GSH (5 mM) with laser irradiation (808 nm, 0.5 W/cm^2). (i) Comparison of the DHR123 fluorescence intensity in the presence of NPs and GSH with/without irradiation (n = 3).

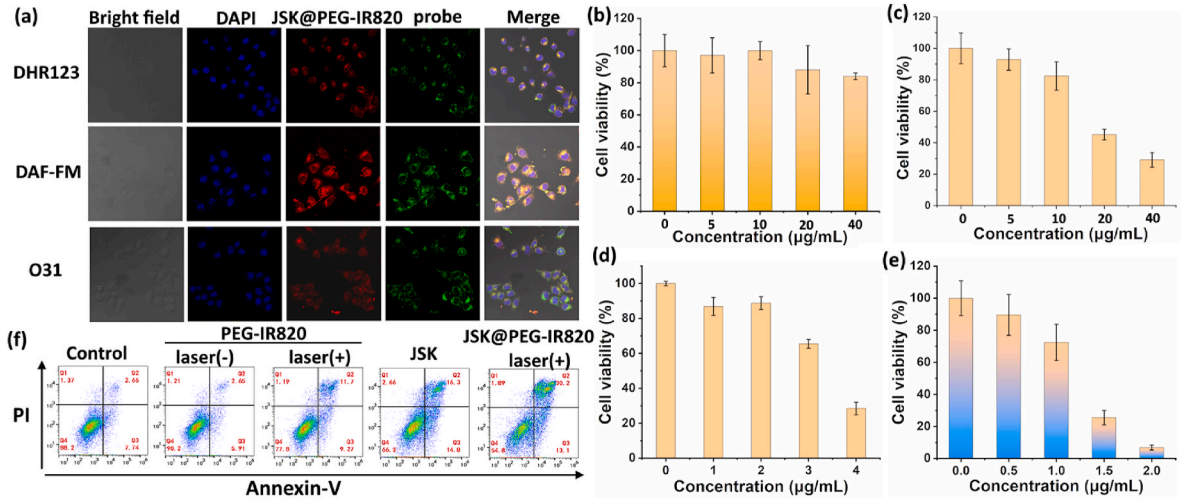

Fig. 3. (a) CLSM imaging of JSK@PEG-IR820 treated with DHR123, DAF-FM and O31 probe, showing the effective generation of superoxide radical, NO and $ONOO^-$ respectively. (b) MTT assay of U87MG cells treated with PEG-IR820 only, (c) PEG-IR820 with laser (808 nm, 8 min, 0.5 W/cm^2), (d) JSK only and (e) JSK@PEG-IR820 with laser irradiation (808 nm, 8 min, 0.5 W/cm^2). (f) Flow cytometry U87MG cells treated of PEG-IR820 with/without irradiation, JSK and JSK@PEG-IR820 with irradiation (808 nm, 8 min, 0.5 W/cm^2).

strong green signals resulting from the activation of DAF-FM and O31, respectively (Fig. 3a), consistent with the results obtained in the aqueous solution.

Due to the high phototoxicity of JSK@PEG-IR820 NPs, we assessed cell viability by treating U87MG cells with PEG-IR820 with/without irradiation, JSK alone, and JSK@PEG-IR820 with irradiation, respectively. PEG-IR820 is inherently non-cytotoxic, as evidenced by the consistently high cell viability (Fig. 3b), whereas laser irradiation led to a significant increase in cell death (Fig. 3c), which can be attributed to the high production of superoxide radicals. The induction of NO by JSK contributed to a low half-maximal inhibitory concentration of only 3.2 μg/mL. Consequently, the synergistic effect is responsible for the enhanced phototherapeutic efficacy of JSK@PEG-IR820, resulting in a lower IC_{50} of 1.4 μg/mL. We further investigated the therapeutic efficacy of JSK@PEG-IR820 NPs in hypoxic conditions, and the phototoxicity under 2 % O_2 atmosphere remained very high (Fig. S5). The calcein-AM/PI co-staining experiment result is consistent with that of the MTT assay, indicating the excellent phototoxicity of JSK@PEG-IR820 with the help of laser (Fig. S6).

To further investigate the apoptosis induced by ROS/RNS, flow cytometry was employed (Fig. 3f). Similar to the MTT assay, cellular apoptosis was nearly negligible in the group treated with PEG-IR820 alone compared to the control group, indicating the low dark toxicity of PEG-IR820 itself. The number of apoptotic cells increased with laser irradiation, resulting in an apoptosis rate of 20.9 %. This effect was even more pronounced in the group treated with JSK (31.1 %). Notably, the group treated with JSK@PEG-IR820 with laser irradiation exhibited a significantly higher apoptotic rate of 43.3 %. These results collectively

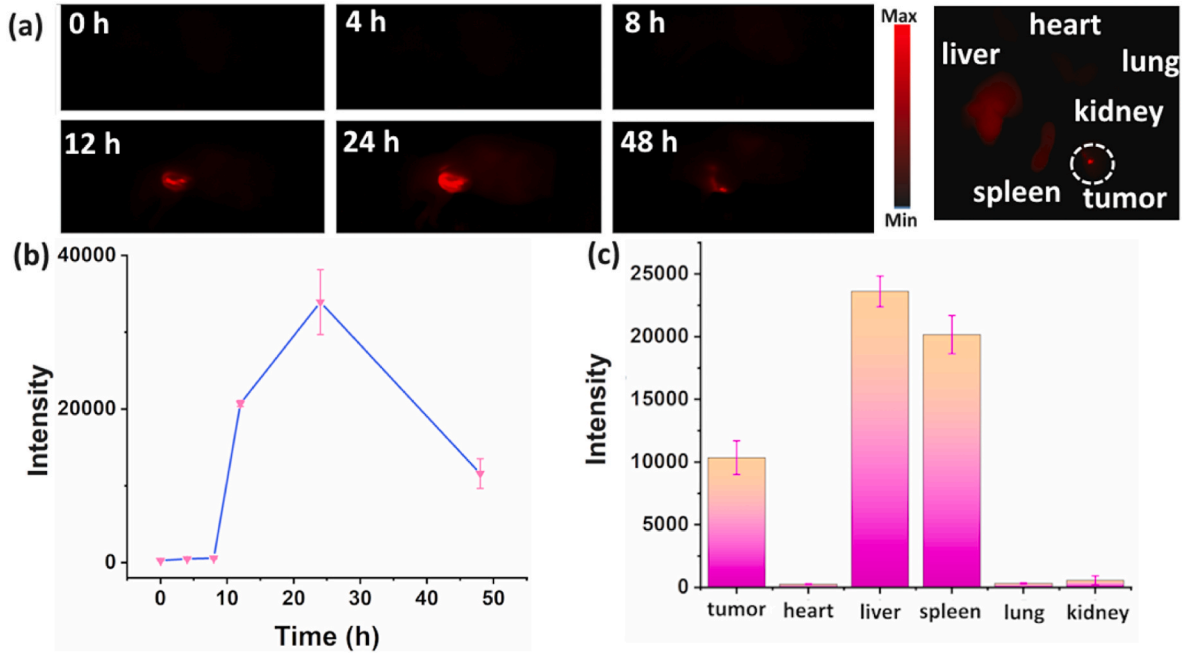

Fig. 4. (a) NIR-II fluorescence imaging of U87MG tumor bearing mice upon excitation at 808 nm at different time intervals (0, 4, 8, 12, 24 and 48 h) and the *ex-vivo* fluorescence imaging of the tumor and main organs. The tumor was circled with white dashed line. (b) Tumor fluorescence intensity change at different time intervals (n = 3). (c) Quantification of the fluorescence intensity of tumor, heart, liver, lung, kidneys and spleen of the sacrificed nude mice after 48 h injection (n = 3).

underscore the potential of these nanoparticles for enhancing type I PDT through NO gas therapy.

3.4. *In vivo NIR-II fluorescence imaging-guided NO therapy enhanced type I PDT*

To investigate the time-dependent accumulation of JSK@PEG-IR820 *in vivo*, we intravenously administered the nanoparticles to mice bearing U87MG tumors and recorded fluorescence images at various time intervals (0, 4, 8, 12, 24, and 48-h). JSK@PEG-IR820 exhibited passive tumor targeting, primarily attributed to the well-established enhanced permeability and retention (EPR) effect (Fig. 4a). Notably, at the 24-h post-injection mark, the tumor displayed the highest fluorescence signal, suggesting that this time point is the most suitable for laser irradiation (Fig. 4b). Subsequently, after 48 h, the mice were sacrificed, and the fluorescence intensity of key organs including the heart, lungs, liver, kidneys, and spleen was quantified (Fig. 4c). The results indicated that the fluorescence intensity in the tumor was weaker than that observed in the liver or spleen.

Driven by the guidance provided by NIR-II imaging, we conducted further investigations into the phototherapeutic efficacy. Nude mice bearing U87MG tumors were divided into five groups: a control group receiving saline with irradiation, groups treated with PEG-IR820 with or without irradiation, a JSK@PEG-IR820 group, and a group treated with JSK@PEG-IR820 with irradiation. Following intravenous administration of the respective materials, the mice in the PEG-IR820 and JSK groups were not subjected to exceptional irradiation, whereas those in the other three groups underwent laser treatment. Over the course of the study, we recorded changes in body weight and tumor volume (Fig. 5a and b).

Remarkably, despite laser irradiation, tumors in the control group and the PEG-IR820-treated group exhibited rapid proliferation, indicating the low dark toxicity of PEG-IR820. In contrast, groups treated with PEG-IR820 (+laser) or JSK displayed significant tumor suppression, with noteworthy complete tumor regression observed in the JSK@PEG-IR820 + laser group (Fig. 5a and Fig. S7). The increase in the body weight of mice after treatment suggested minimal adverse effects, highlighting the low toxicity of the nanoparticles (Fig. 5b). Afterwards, we conducted H&E staining, TUNEL staining, HIF-1α, and Ki67 staining analyses on the sacrificed mice after treatment. Both H&E and TUNEL staining analyses demonstrated that the phototherapeutic effect of PEG-IR820 effectively induced cell death. The combined effect of oxygen consumption and PDT/NO therapy resulted in blood vessel damage, leading to inadequate oxygen and nutrient supply in the tumor microenvironment.

Further evidence of the biocompatibility of JSK@PEG-IR820 NPs was provided through H&E staining analysis of normal organs (heart, liver, lung, spleen, and kidney) (Fig. S8). The cell nuclei in these organs remained normal, indicating low toxicity. Additionally, we recorded various hematological parameters, including red blood cell count, white blood cell count, platelet count, lymphocyte count, albumin levels, glucose levels, aspartate aminotransferase, alanine aminotransferase, alkaline phosphatase, total protein, blood urea nitrogen, and creatinine (Fig. 5d-l and Figs. S9–S11). The results showed no adverse effects on blood circulation, as the parameters remained similar to those in the control groups.

Given that JSK@PEG-IR820 NPs accumulated in the liver, as indicated by NIR-II fluorescence imaging, we assessed liver function parameters, including aspartate aminotransferase, alkaline phosphatase, alanine aminotransferase, and total protein. These parameters were maintained at normal levels (Fig. 5g-j), suggesting intact liver function. Furthermore, blood urea nitrogen and creatinine levels (Fig. 5k and l), essential indicators of renal function, indicated negligible side effects of the NPs on renal function. In summary, JSK@PEG-IR820 NPs demonstrated high biocompatibility as a nanomedicine for cancer phototheranostics.

4. Conclusions

In summary, our approach simultaneously achieves the goals of "broadening sources" to enhance $O_2^{-\cdot}$ generation and "reducing expenditure" to diminish $O_2^{-\cdot}$ consumption. The rational design of the JSK@PEG-IR820 nanosystem not only amplifies intermolecular electron transfer for type I PDT but also initiates NO gas therapy through GSH consumption. This dual-action approach contributes significantly to enhanced phototherapeutic efficacy, thanks to the generation of

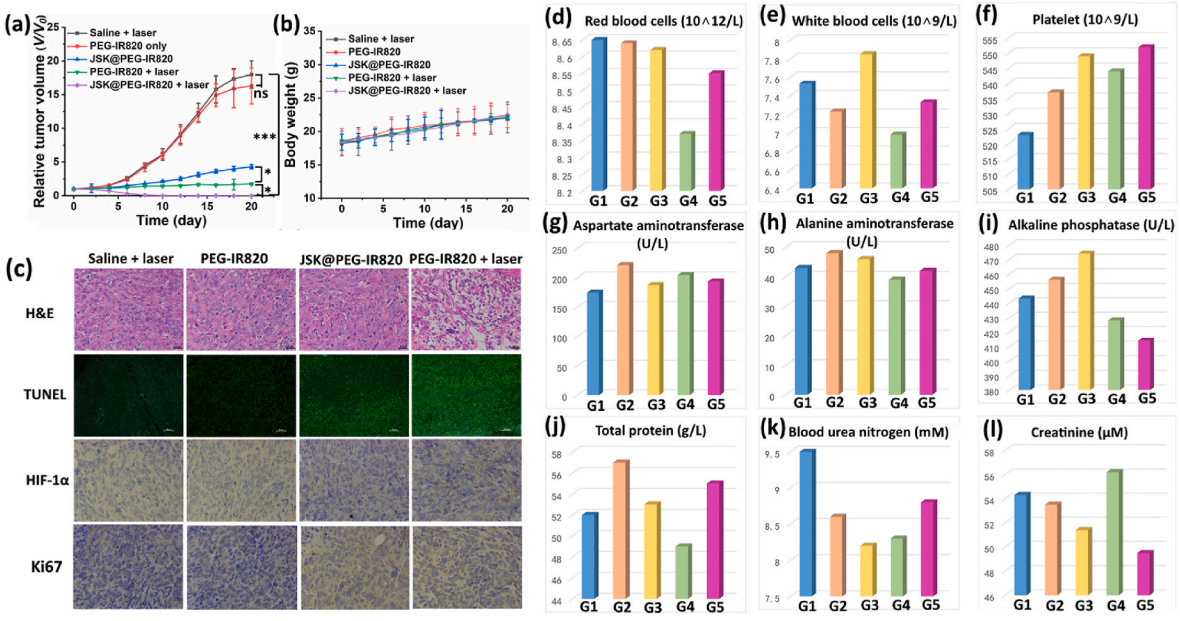

Fig. 5. (a) Relative tumor volume of the mice in each group during treatment, (b) Body weight change of the mice, (c) H&E, TUNEL, HIF-1α and Ki67 staining pictures of the tumors. (d) Red blood cells, (e) white blood cells, (f) platelet, (g) aspartate aminotransferase; (h) alanine aminotransferase, (i) alkaline phosphatase, (j) total protein, (k) blood urea nitrogen, (l) creatinine parameters of the mice in each group. G1: Saline + laser; G2: PEG-IR820 only; G3: JSK@PEG-IR820; G4: PEG-IR820 + laser (808 nm, 0.5 W/cm^2); G5: JSK@PEG-IR820 + laser (808 nm, 0.5 W/cm^2).

$ONOO^{-\cdot}$ with superior cytotoxicity. Utilizing NIR-II imaging as a guide, this intelligent nanosystem serves as a navigation tool for tumor localization and exhibits pH-responsive JSK release. Furthermore, our research demonstrates complete inhibition of tumor growth, with no adverse effects observed in normal organs, underscoring the biocompatibility of this nanomedicine. This work represents a pioneering example of gas therapy-sensitized type I PDT for advanced phototheranostics.

Ethical approval and concent to participate

Approval for animal experimentation was obtained from the Animal Center of Nanjing Normal University, Nanjing, China (IACUC-20230226). No consent to participate is needed because this study is human exclusive.

CRediT authorship contribution statement

Jianhua Zou: Writing – original draft, Investigation, Conceptualization. **Zheng Li:** Investigation. **Yang Zhu:** Investigation. **Yucen Tao:** Investigation. **Qing You:** Investigation. **Fangfang Cao:** Investigation. **Qinghe Wu:** Investigation. **Min Wu:** Investigation. **Junjie Cheng:** Investigation. **Jianwei Zhu:** Investigation. **Xiaoyuan Chen:** Writing – review & editing, Supervision, Funding acquisition, Conceptualization.

Declaration of competing interest

The authors declare that they have no known competing financial interests or personal relationships that could have appeared to influence the work reported in this paper.

Acknowledgement

The authors acknowledge the financial support from the National University of Singapore (NUHSRO/2020/133/Startup/08, NUHSRO/2023/008/NUSMed/TCE/LOA, NUHSRO/2021/034/TRP/09/Nanomedicine), National Medical Research Council (MOH-001388-00, MOH-001041, CG21APR1005), Singapore Ministry of Education (MOE-000387-00), National Research Foundation (NRF-000352-00) and the Open Fund Young Individual Research Grant of Singapore (MOH-001127-01).

Appendix A. Supplementary data

Supplementary data to this article can be found online at https://doi.org/10.1016/j.bioactmat.2023.12.023.

References

[1] a) W. Fan, P. Huang, X. Chen, Chem. Soc. Rev. 45 (2016) 6488–6519; b) X. Li, N. Kwon, T. Guo, Z. Liu, J. Yoon, Angew. Chem. Int. Ed. 57 (2018) 11522–11531.
[2] Z. Zhou, J. Song, L. Nie, X. Chen, Chem. Soc. Rev. 45 (2016) 6597–6626.
[3] a) J. Cheng, Y. Zhu, Y. Dai, L. Li, M. Zhang, D. Jin, M. Liu, J. Yu, W. Yu, D. Su, J. Zou, X. Chen, Y. Liu, Angew Chem. Int. Ed. Engl. 62 (2023) e202304312; b)X. Hu, C. Zhu, F. Sun, Z. Chen, J. Zou, X. Chen, Z. Yang, Adv. Mater. 2023, e2304848. c) Z. Li, J. Zou, X. Chen, Adv. Mater. 35 (2023) e2209529; d) J. Zhu, Y. Zhang, Z. Li, X. Bao, Y. Zhou, B. Ma, Y. Xie, P. Yan, Z. Wu, Q. Zhang, J. Zou, X. Chen, Mater. Horiz. 10 (2023) 3014–3023.
[4] a) J. Zou, L. Li, Z. Yang, X. Chen, Nanophotonics 10 (2021) 3229–3245; b) J. Zou, L. Li, J. Zhu, X. Li, Z. Yang, W. Huang, X. Chen, Adv. Mater. 33 (2021) e2103627; c) J. Zou, J. Zhu, Z. Yang, L. Li, W. Fan, L. He, W. Tang, L. Deng, J. Mu, Y. Ma, Y. Cheng, W. Huang, X. Dong, X. Chen, Angew. Chem. Int. Ed. 59 (2020) 8833–8838.
[5] a) W. Tang, Z. Yang, L. He, L. Deng, P. Fathi, S. Zhu, L. Li, B. Shen, Z. Wang, O. Jacobson, J. Song, J. Zou, P. Hu, M. Wang, J. Mu, Y. Cheng, Y. Ma, L. Tang, W. Fan, X. Chen, Nat. Commun. 12 (2021) 523; b) C. Ratanatawanate, A. Chyao, K.J. Balkus Jr., J. Am. Chem. Soc. 133 (2011) 3492–3497.
[6] H. Deng, Z. Zhou, W. Yang, L.S. Lin, S. Wang, G. Niu, J. Song, X. Chen, Nano Lett. 20 (2020) 1928–1933.
[7] Y. Wang, Y. Liu, H. Sun, D. Guo, Coord. Chem. Rev. 395 (2019) 46–62.
[8] a) W. Chen, Z. Wang, M. Tian, G. Hong, Y. Wu, M. Sui, M. Chen, J. An, F. Song, X. Peng, J. Am. Chem. Soc. 145 (2023) 8130–8140; b) G. Lan, K. Ni, S.S. Veroneau, X. Feng, G.T. Nash, T. Luo, Z. Xu, W. Lin, J. Am. Chem. Soc. 141 (2019) 4204–4208; c) L. Li, C. Shao, T. Liu, Z. Chao, H. Chen, F. Xiao, H. He, Z. Wei, Y. Zhu, H. Wang, X. Zhang, Y. Wen, B. Yang, F. He, L. Tian, Adv. Mater. 32 (2020) e2003471; d) X. Li, D. Lee, J.D. Huang, J. Yoon, Angew Chem. Int. Ed. Engl. 57 (2018) 9885–9890; e) Y. Li, D. Zhang, Y. Yu, L. Zhang, L. Li, L. Shi, G. Feng, B.Z. Tang, ACS Nano 17 (2023) 9110–9125; f) Y.C. Liu, G.J. Liu, W. Zhou, G.L. Feng, Q.Y. Ma, Y. Zhang, G.W. Xing, Angew Chem. Int. Ed. Engl. (2023) e202309786; g) J. Tong, A. Liu, S. Huang, Y. Yao, G.G. Shan, Z.M. Su, Chem. Asian J. 18 (2023) e202300175; h) H. Wang, T. Qin, W. Wang, X. Zhou, F. Lin, G. Liang, Z. Yang, Z. Chi, B.Z. Tang, Adv. Sci. 10 (2023) e2301902.
[9] a) Z. Wang, A. Jin, Z. Yang, W. Huang, ACS Nano 17 (2023) 8935–8965; b)Y. Yu, L. Xiang, X. Zhang, L. Zhang, Z. Ni, Z. H. Zhu, Y. Liu, J. Lan, W. Liu, G. Xie, G. Feng, B. Z. Tang, Adv. Sci. 2023, e2302395. c) T. Zhang, Y. Pan, M. Suo, M. Lyu, J.W.Y. Lam, Z. Jin, S. Ning, B.Z. Tang, Adv. Sci. (2023) e2304042; d)M. Zhao, Y. Zhang, J. Miao, H. Zhou, Y. Jiang, Y. Zhang, M. Miao, W. Chen, W. Xing, Q. Li, Q. Miao, Adv. Mater. 2023, e2305243. e) D. Zhu, T. Zhang, Y. Li, C. Huang, M. Suo, L. Xia, Y. Xu, G. Li, B.Z. Tang, Biomaterials 283 (2022) 121462; f) J. Zhuang, B. Wang, H. Chen, K. Zhang, N. Li, N. Zhao, B.Z. Tang, ACS Nano 17 (2023) 9110–9125.
[10] a) D. Riccio, M. Schoenfisch, Chem. Soc. Rev. 41 (2012) 3731–3741; b) K. Sharma, H. Chakrapani, Nitric Oxide 43 (2014) 8–16.
[11] a) W. Fan, N. Lu, P. Huang, Y. Liu, Z. Yang, S. Wang, G. Yu, Y. Liu, J. Hu, Q. He, J. Qu, T. Wang, X. Chen, Angew Chem. Int. Ed. Engl. 56 (2017) 1229–1233; b) C. Fowley, A.P. McHale, B. McCaughan, A. Fraix, S. Sortino, J.F. Callan, Chem. Commun. 51 (2015) 81–84; c) A. Fraix, M. Blangetti, S. Guglielmo, L. Lazzarato, N. Marino, V. Cardile, A. C. Graziano, I. Manet, R. Fruttero, A. Gasco, S. Sortino, ChemMedChem 11 (2016) 1371–1379; d) R. Guo, Y. Tian, Y. Wang, W. Yang, Adv. Funct. Mater. 27 (2017); e) T. Horinouchi, H. Nakagawa, T. Suzuki, K. Fukuhara, N. Miyata, Bioorg. Med. Chem. Lett 21 (2011) 2000–2002; f) T. Horinouchi, H. Nakagawa, T. Suzuki, K. Fukuhara, N. Miyata, Chemistry 17 (2011) 4809–4813; g) Z. Jin, Y. Wen, Y. Hu, W. Chen, X. Zheng, W. Guo, T. Wang, Z. Qian, B.L. Su, Q. He, Nanoscale 9 (2017) 3637–3645; h) J. Mu, C. Li, Y. Shi, G. Liu, J. Zou, D.Y. Zhang, C. Jiang, X. Wang, L. He, P. Huang, Y. Yin, X. Chen, Nat. Commun. 13 (2022) 2513.
[12] P.C. Ford, Nitric Oxide 34 (2013) 56–64.
[13] a) J. Xu, F. Zeng, H. Wu, C. Hu, C. Yu, S. Wu, Small 10 (2014) 3750–3760; b) J. Xu, F. Zeng, H. Wu, S. Wu, J. Mater. Chem. B 3 (2015) 4904–4912; c) M. Zhang, H. Jin, Y. Liu, L. Wan, S. Liu, H. Zhang, Acta Biomate 169 (2023) 517–529; d) X.F. Zhang, S. Mansouri, D.A. Mbeh, L. Yahia, E. Sacher, T. Veres, Langmuir 28 (2012) 12879–12885; e) E.Y. Zhou, H.J. Knox, C.J. Reinhardt, G. Partipilo, M.J. Nilges, J. Chan, J. Am. Chem. Soc. 140 (2018) 11686–11697.
[14] a) P. Pei, Y. Chen, C. Sun, Y. Fan, Y. Yang, X. Liu, L. Lu, M. Zhao, H. Zhang, D. Zhao, X. Liu, F. Zhang, Nat. Nanotechnol. 16 (2021) 1011–1018; b) T. Wang, S. Wang, Z. Liu, Z. He, P. Yu, M. Zhao, H. Zhang, L. Lu, Z. Wang, Z. Wang, W. Zhang, Y. Fan, C. Sun, D. Zhao, W. Liu, J.G. Bunzli, F. Zhang, Nat. Mater. 20 (2021) 1571–1578; c) Y. Liu, Y. Li, S. Koo, Y. Sun, Y. Liu, X. Liu, Y. Pan, Z. Zhang, M. Du, S. Lu, X. Qiao, J. Gao, X. Wang, Z. Deng, X. Meng, Y. Xiao, J.S. Kim, X. Hong, Chem. Rev. 122 (2022) 209–268.